Coupled Solution of 3D Unstructured Finite Volume Discretizations of the RANS Equations on Q2 Primal and Dual Grids. Application to the 4 th High Lift Prediction Workshop

Jean-Marie Le Gouez

Coupled Solution of 3D Unstructured Finite Volume Discretizations of the RANS Equations on Q2 Primal and Dual Grids. Application to the 4th High Lift Prediction Workshop.

Jean-Marie Le Gouez[1]
Onera, Châtillon, 92320, France

This paper describes the main features of NextFlow ITW, a high-order reconstructed Finite Volume solver for turbulent flows of perfect gases. This code of the 'k-exact' family was worked out on the occasion of the High-Lift Prediction Workshop 4, it is based on reconstructed k1 to k3 polynomials and results in 2nd order and 3rd order FV schemes. One important characteristic is that it couples the discretization of the RANS equations on the unstructured primal grid (a multi-element grid with prisms, pyramids and tetrahedron) and on its dual grids (made of vertex-, edge- and face-centered Finite Volumes). 3 series of runs proposed by the Workshop were conducted with this solver and its 2D reduced version, their set-up are described together with detailed results. Reference is made to the synthesis of all submissions prepared by the coordinator of the HO Technology Focus Group and the Workshop organizers.

I. Introduction

We present shortly the main features of a prototype 'k-exact' reconstructed Finite Volume solver that was used to conduct a series of test-cases in the framework of the High Lift Prediction Workshop 4.

Two main features were improved on this occasion:

- the polynomial reconstruction from a discrete field of curvilinear volume integrals that extends over a stencil of quadratic (Q2) cells,
- the coupling of the discretization on primal and dual overset grids, which represents the interwoven feature [1] [2] of this code NextFlow ITW.

The robustness of these schemes and their predictive abilities on this type of complex geometry and flow is to be discussed. For this, the CLmax study (case 2a) and the grid convergence analysis (case1b) of the HLPW 4 were conducted, with reconstructions from degree 1 to 3, depending on the extent of the stencils and the user's choice.

The simpler 2D version acting only on the primal unstructured multi-element grid was used to perform the verification case from the TMR site [3]. Due to difficulties in converging to the RANS solution with the SA-Neg. turbulence model, when using higher order reconstructions, 2D URANS cases were done in comparison.

II. Main Features of the NextFlow ITW solver

This solver is a FORTRAN 95 code, with a single degree of freedom per conservation equation and per Q2 Finite Volume. It uses a polynomial reconstruction of any variable field in each Finite Volume from the discrete volume averages of this field in a set of Finite Volumes that surround it, its 'stencil'. On curvilinear Q2 (quadratic) grids, the discrete fields in the stencils that drive the reconstruction through Weighted Least Squares are considered as curvilinear volume integrals. The reconstructed polynomial over the stencil is then evaluated on each interface of the central FV, as its curvilinear surface integrals.

[1] CFD Developer, ONERA Department of Aerodynamics, Aeroacoustics, Aeroelasticity

On a given interface, it provides to the approximate Riemann solver 2 sets of conservative variables, from the reconstructions and projections in its left and right FV stencils. The degree of the reconstruction polynomial varies from 1 to 3, on a complete basis of 20 monomials in the global reference frame. This weighted least square fit of the polynomial integrals to the stencil discrete values is considered robust if the stencil has 50% more FVs than the basis size. Stencils of 15 FVs permit a k2 reconstruction, and k3 is enabled with 30 FVs.

The novel 3D version of the solver uses a quadratic geometry of the FVs, each interface of them is represented by a set of adjacent Q2 patches (triangles or quadrangles with 6 and 9 nodes). This permits to represent also the dual grids in the HO NGON format, which was developed for control volumes having an arbitrary number of discrete interfaces.

This solver operates on overset grids, they are assembled at the user's choice among:

1) the primal grid of multi-element type (prisms, pyramids, tetrahedrons), for the High Lift prediction test cases we used the POINTWISE P-T Q2 series,
2) its median node dual grid, also a Q2 grid, where each interface of a dual FV is the union of Q2 quadrangles identified in each primal FV around the edge that links the central node of this dual FV to an adjacent node,
3) its edge-dual grid; a FV is built around each edge of the primal grid, by identifying in a primal cell the triangle of communication between the fractions of the cell volume allotted to 2 adjacent edges sharing a node,
4) its face-dual grid (commonly called the diamond grid); 2 adjacent faces of a primal cell, sharing an edge, communicate also through a quadratic triangle, the 6 nodes that describe this triangle are obtained for given values of the parametric coordinates of the Q2 primal FV. The result of the build-up of this envelope is a face-dual FV made, depending if the face is a quad or a triangle, of:
   - ✓ 2 abutting pyramids with this face as a common base and the centroid of a primal cell as the 5^{th} node,
   - ✓ 2 abutting tets with this face as a common base and the centroid of a primal cell as the 4^{th} node.

All these grids presented in NGON format are considered as the support of the same cell-centered FV scheme. Each grid is autonomous; a turbulent flow simulation of perfect gas can be performed on each independently, in the same executable. These discretizations can also be coupled, through composite reconstruction stencils.

The FV samples that serve for the polynomial fit, besides the first or second direct neighbors in a given grid, can also be agglomerated from grids of other kind. For this we use the standard connectivity table: node to element, but also the derived ones, edge to element and face to element, after numbering uniquely the edges and faces of the primal grid.

All the overset grid combinations were programmed in the preprocessor for the spatial scheme of NextFlow-ITW. After the construction of the composite stencils, the discrete operators for the reduction of the fields from the stencils volume data to the interface are coded. For each interface of an active grid, they provide 8 tables of linear combination coefficients [1], the application of which results in:

- ✓ an extrapolation from the left (over the stencil of the left FV and a linear basis k1),
- ✓ an extrapolation from the right (over the stencil of the right FV and a linear basis k1),
- ✓ 2 extrapolations, resp. from the left and the right, over the same stencils and bases of higher degree k2 or k3,
- ✓ evaluations of the interface centered average of the components of the gradient, over a higher degree basis and the union of the left and right stencils (3 tables),
- ✓ an evaluation of a finite difference of order 3 for the artificial dissipation operator. 2 options are available, as this table can be obtained from the surface integral of the 3^{rd} normal derivative of the reconstructed polynomial, if a k3 fit was possible, or be the difference of 2 evaluations of second differences over respectively the left and right stencil.

These tables are used successively for the fields of conservative and primitive variables, or the components of the flux density tensor. These derived fields are computed in each cell of the stencil from the mean conservative variables. The reconstruction of the flux density tensor is used in an option for a centered scheme stabilized by a high order artificial dissipation [2] that was not used in this application study.

The comparison of the current variation range of the fields over the stencil or obtained from left and right over a linear or a higher degree reconstruction serve for an equivalent slope limiter.

III. 3D grids for the CRM High-Lift configuration

We have used the quadratic multi-element grids prepared by POINTWISE for the HO TFG (Technology Focus Group) [4] of the HLPW4 workshop [5]. For each surface grid refinement level, i.e. coarse, medium and fine, different

3D grids in terms of thickness of the wall cells were generated. The ones that we selected are: y+ = 100, 200, 800 [4]. None of our computations used the available extra-fine grids.

These grids are labelled P-T Q2, they use prisms layers on the majority of walls, connected to pyramids and then tetrahedron in the rest of the volume. Some regions of the fuselage, away from the wing, use quadrilaterals as the surface grid. A specific preprocessor of our solution conducts a 2-level partitioning of these grids, and then in each sub-partition containing of the order of 200 primal cells, Q2 dual grids are created in the NGON format.

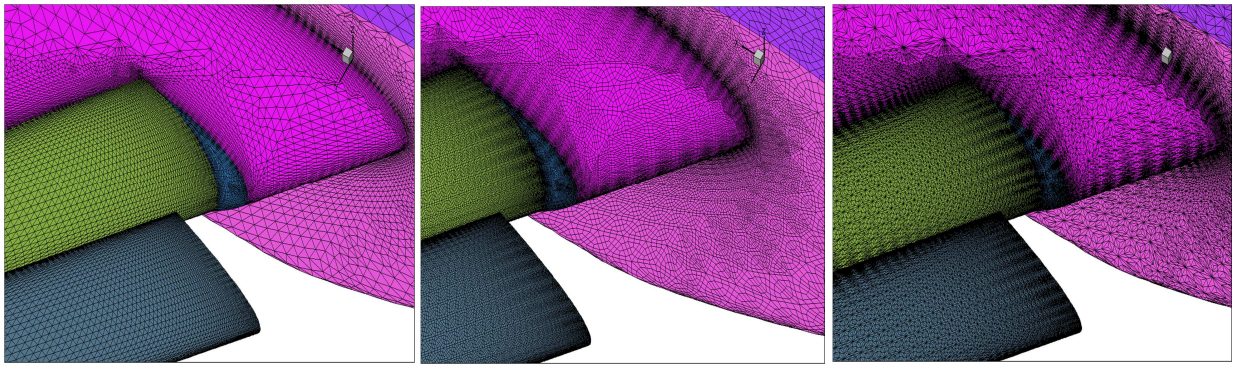

Fig. 1 Surface grids of the family POINTWISE P-T Q2 medium and its node- and edge-duals.

Each quadratic interface is represented by 4 linear elements (tri. or quad.).

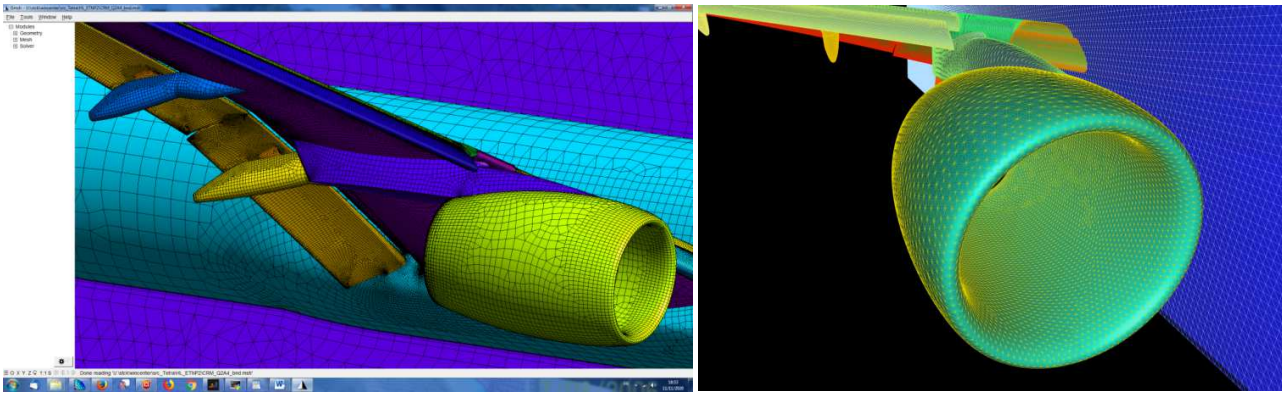

Fig. 2 Surface grids; left at the coarse level (primal), right at the medium level (edge-dual).

The k3 reconstructions that were cited in the preceding chapter can only be computed in the prismatic regions for stencils of cells with an aspect ratio below 200, and their accuracy also is sensitive to the element curvature. In the preprocessor of the spatial scheme, in order to obtain polynomial continuous representations from the discrete fields, a linear system must be solved, the order of which is the size of the polynomial basis. There are criteria to be met on the condition number of this linear system and on the resulting diagonal dominance of the projected polynomial on cell interfaces. They are satisfied at present for the HLPW4 grids of the type “Log-law of the wall” with a target y+ over 50.

By using the graph partitioner METIS successively at two levels, with a first partitioning of the primal grid into 64 to 256 blocks, each partitioned again into 64 to 256, we obtain between 4096 and 32768 cell groups, see Fig. 3a and 3b. On Fig. 3b, the node-dual grid of a sub-partition is shown, where its continuity over the prisms, pyramids and tets layers is evidenced. The sub-partitions comprise each of the order of 300 to 1000 FVs, when the dual grids are overset to the primal ones. On Fig. 3c and 3d are represented, with a shift in space for clarity, the 4 overset (interwoven) grids of 2 types of sub-partitions, one away from the walls, the other inside the near wall cell layers.

These overset grids in a sub-partition are clustered into a single one for the solver, they occupy of the order of 6 Mbytes of memory and fit in the caches of recent CPUs. Not shown on Fig 3b to 3d are the 2 layers of ghost cells at the periphery of each sub-partition to couple the resolution with other sub-partitions grids. These ghost cells may either be duplicated or exchange data in shared memory.

For this study, the computations were done on a single node AMD EPYC Rome with 2 processors of 32 cores each. With a memory of 256 GBytes, up to 46 Mdof/eqn could be computed. All the transfer of information from the ghost

cells was then done in shared memory, without duplication, showing a high memory bandwidth. The processing of the sub-partitions was distributed to the cores by 2 OpenMP nested loops for the 2 partition levels, over 8 NUMA nodes.

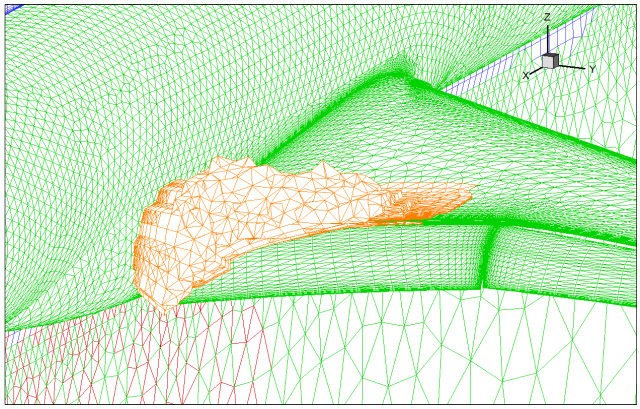

Fig. 3a First level of partitioning.

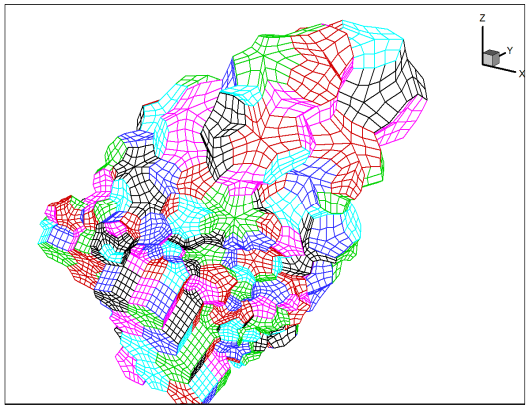

Fig. 3b Node-dual grid of a sub-partition.

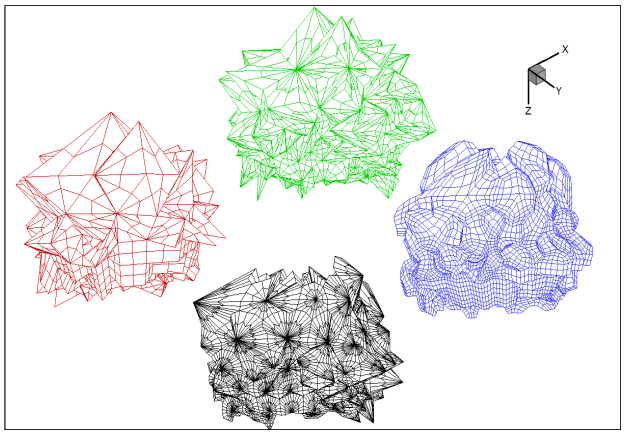

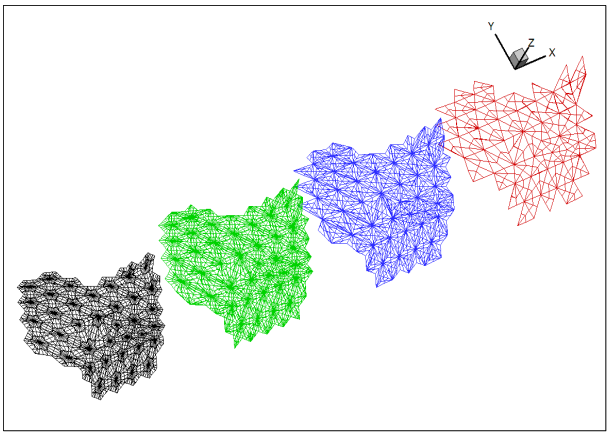

Fig. 3c and 3d Exploded views of the overset grids of 2 representative sub-partitions.

Among all the possible combinations of activation and coupling of the overset grids solutions, only 3 have been tested, labelled: 2G, 3G and 4G, with the primal grid and the node-dual one always active. In 3G mode, the edge-dual coupled solution is added, in 4G also the face-dual grid and solution expand the coupled solver.

With the 3 refinement levels of the POINTWISE Q2 grids: coarse, medium and fine, depending on the active grid options, the runs were done on 1.8 to 46 MFVs, and the same number of dof/eqn. For the y+ 100 primal grids, table 1 summarizes this.

Pointwise P-T Q2 Refinement level ➔	Coarse	Medium	Fine
Primal (cell)	1.3 M	6.9 M	15.0 M
node-dual	0.45 M	2.7 M	5.5 M
edge-dual	2.1 M	11.9 M	25.2 M
face-dual	3.0 M	16.1 M	34.7 M
Total cell+node (2G)	1.8 M	9.6 M	20.5 M
Total cell+node+edge (3G)	3.9 M	21.5 M	45.7 M
Total cell+node+edge+face (4G)	6.9 M	37.6 M	Not used

Table 1 Total number of dof/eqn for the individual and overset grids, y+ 100 family.

The views of Fig. 4 illustrate the topology of the 4 kinds of overset grids in a 4G run. It is one of the various types of graphical post-processing that were performed, here plotting the isovalues of the vorticity field in a slice, to follow the path and strength of a vortex generated on the lateral plate soldered on the exterior of the engine.

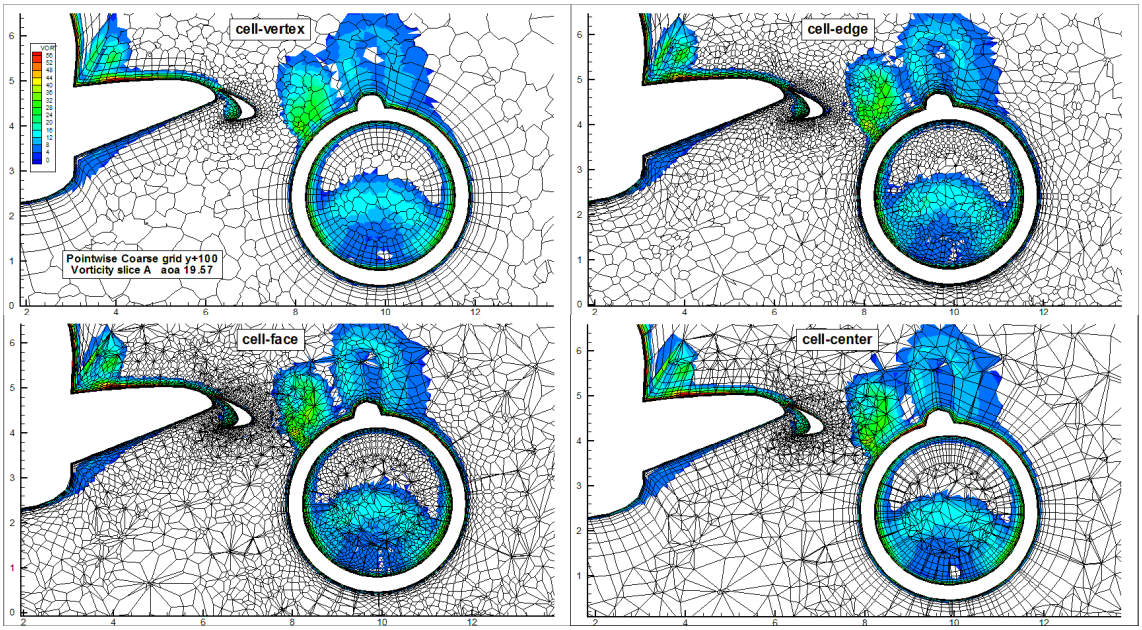

Fig. 4 Views of the vorticity fields in a plane slice across the 4 active grids (if Ω>3). Coarse grid aoa 19.57°.

IV. Results of the test-case 2a of HLPW 4 (CLmax study)

2 series of computations were conducted, each for the 7 angles of incidence from 2.48° to 21.47°. They used the P-T Q2 y+200 medium grid and the P-T Q1 y+100 fine grid (the Q2 fine grid was not yet available at the beginning of the workshop).

The fine grid runs are done on 2 overset grids, cell-center and cell-vertex, for a total of 20.5 Mdof.eqn, while the medium grid runs are over 3G, cell-vertex, cell-edge and cell-center (primal), encompassing 13.2 Mdof/eqn. In this first phase of the workshop, only k1 reconstructions were coded, already on composite stencils.

The forces shown on fig. 5 are the average of those computed on all the active grids. In these runs, the CLmax is found for the incidence of 19.57°, the maximum computed lift is 2.33 on the fine grid. A good agreement is found between the runs on the medium and fine grids, including the difficulty to compute the drag at 19.57° of incidence. The runs on the medium grids are with a lower total count of dofs but 3 overset grids are active.

On Fig. 6, from the workshop committee summary, this result appears in light blue with the HO label (the curve with higher values in the HO category). This result is in-between the majority of RANS 2nd order solvers on one hand, and the Wall-model LES and LBM on the other hand, this last category providing the highest lift figures, together with a RANS computation with an adaptive grid. Our solution is also 2nd order FV at this stage, with the interwoven capability added.

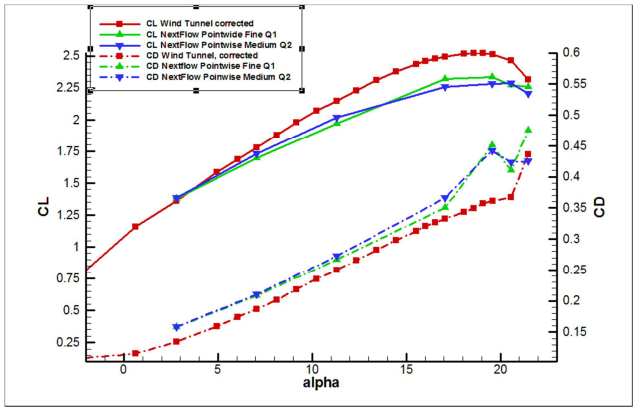

Fig. 5 Clmax study with a k1 reconstruction. Lift and drag coefficients computed and measured.

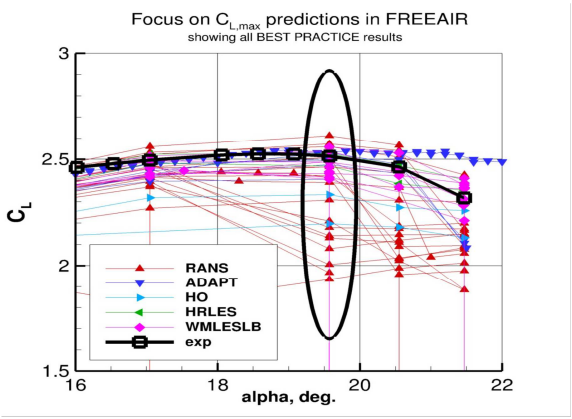

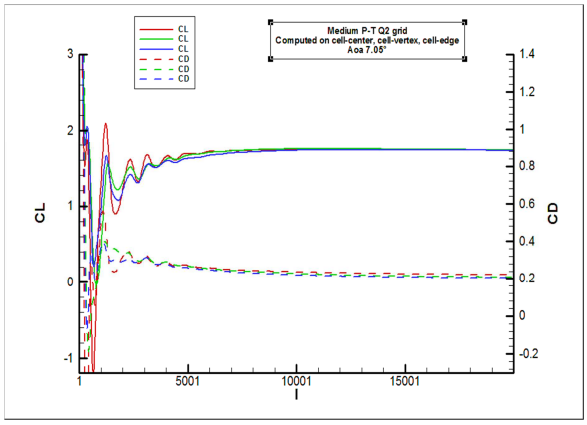

Fig. 6 Clmax study. Zoom on the region of maximal lift **Fig. 7 Computation on the medium grid.**

On fig.7 are plotted the convergence of the lift and drag with the solver explicit iterations and among the overset grids. With these solver settings the iterative convergence is smooth and the overset grid solutions become quickly identical.

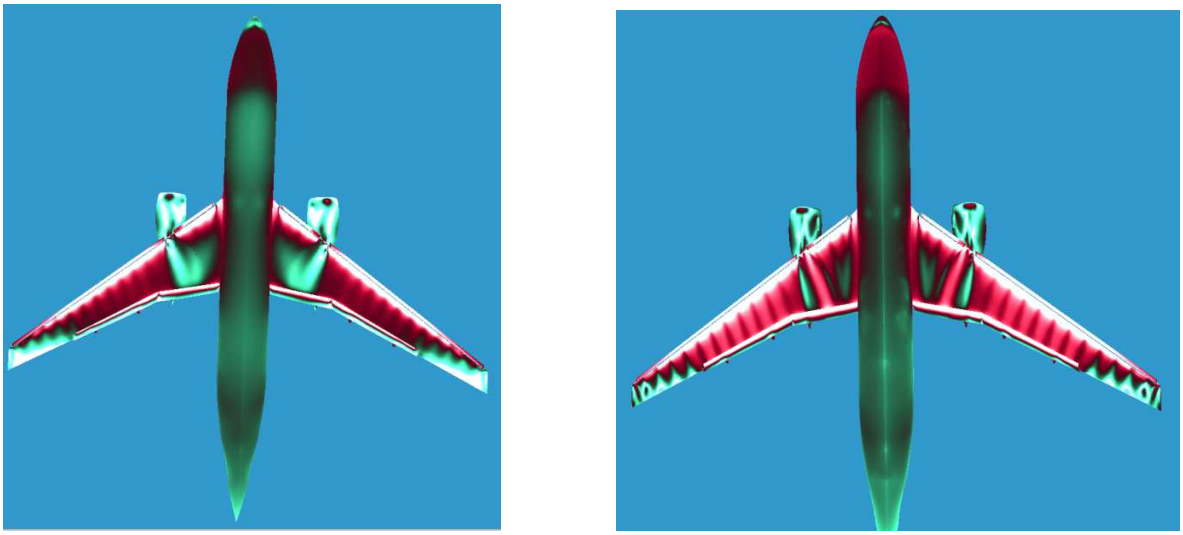

A B

Fig. 8 aoa 7.05°. Wall-extrapolated velocity profile. A on coarse grid 3.9 Mdofs, B on medium grid 13 Mdofs.

Left half-plane cell-vertex solution, Right half-airplane : cell-center solution.

Each of the plots of Fig. 8 shows qualitatively that the solution obtained on 2 coupled grids is very similar. The solution on the cell-vertex grid (half-airplane) is plotted on the symmetrical of its computational grid.

It shows the accuracy of the coupling, in the near-wall FVs, in spite of the fact that the cell-vertex wall cell is twice thinner than the cell-center one. It is also found that some important features of the flow, like the detachment at the outboard side of the wing, are evidenced from the very coarse grid on.

Fig. 9 represents the cp profiles in a slice, for all the computed angles of attack. It shows the contribution of each element of the wing to the Lift. The low lift of the slats for lower aoa is shown, while the contrary occurs for the flaps, they keep a higher lift until 17° of incidence when it decreases earlier near the total Clmax.

In the second phase of the workshop, the first 3rd order FV solutions could be obtained, through a stable k2-k3 reconstruction (k2 or k3 in the various zones of the various grids, depending on the stencil size that can be very different in the prisms and tets zones, and on the user's choice of the stencil depth in a given grid kind, to the 1st or 2nd direct face neighbors). Only a k2 reconstruction can also be imposed even if k3 is locally possible.

These higher order FV solutions where conducted for the test case 1b, grid convergence for the nominal incidence of the flow, some runs at higher incidence were also done. k2 and k3 reconstructions are analoguous to P2 schemes for element based methods, both ks lead to a 3rd order scheme, but with different coefficients of the leading error term.

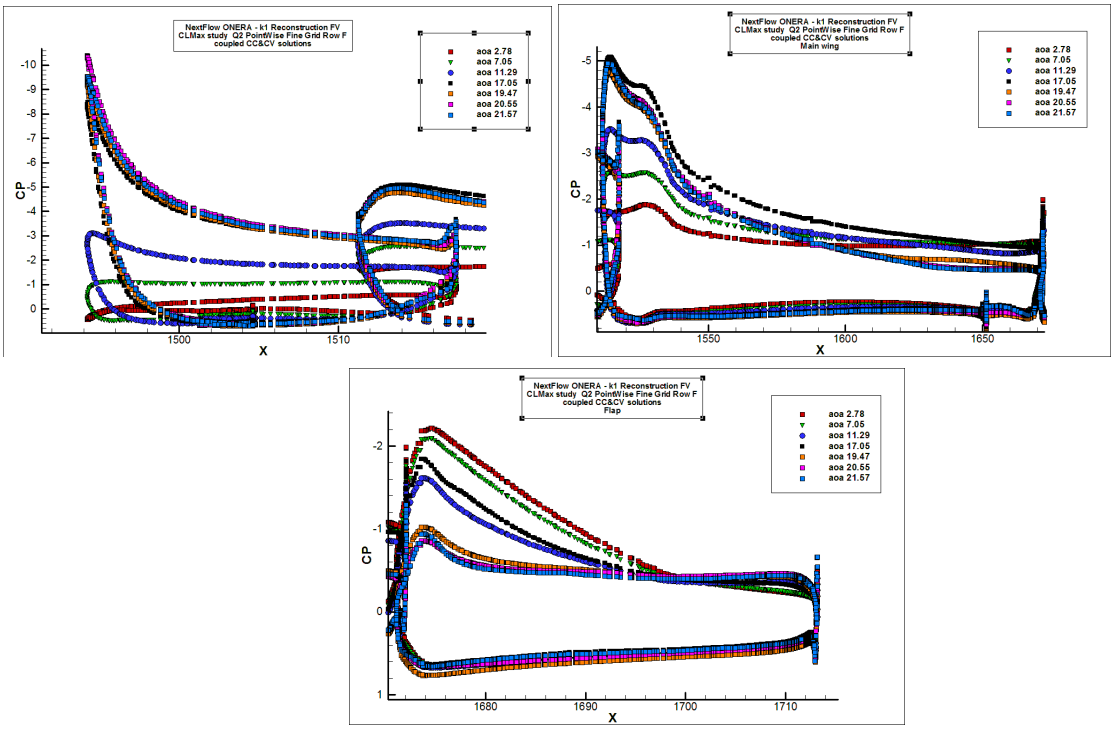

Fig. 9 Clmax study. Cp profiles on the 3 elements for each incidence. Fine grid. Slice F at 65% of the wingspan.

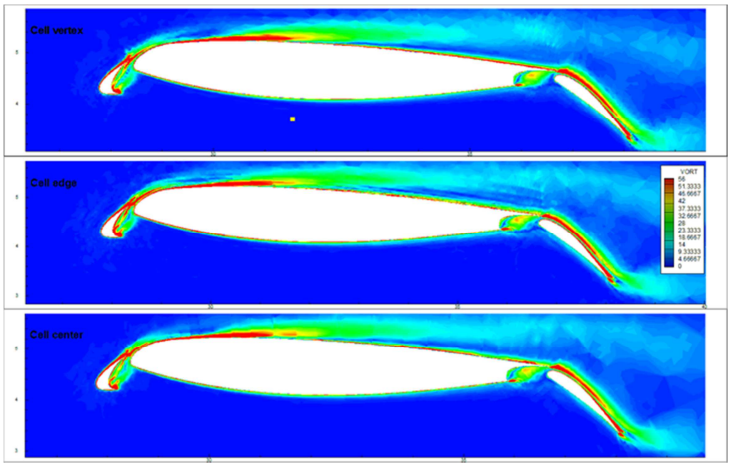

Figure 10 Incidence 19.57° Conformity of the vorticity fields computed simultaneously on 3 active grids..

On Fig. 10, we have plotted the vorticity field on a slice through the coarse grid, computed with a k2 reconstruction on the node-dual, edge-dual and primal grids. The flow detaches at 50% chord on the main element while it remains attached on the flap.

Fig. 11 shows the cp field on the walls in this spatially 3rd order run. Fig. 12 plots the fields of cf at 7.05° incidence, computed at 3rd order on 2 overset grids with respectively 6.9 and 21 Mdof/eqn.

The curves of reduction of the rms residuals for the continuity and momentum equations with the explicit local time-stepping iterations are shown on fig. 13a and b. One case for 3 angles of incidence, 7.05 to 19.57, with a linear reconstruction, is shown on the left plot, a case with the higher aoa is represented on the center plot. The relative reduction of the total energy residuals is very close to that of the continuity equation, for these low Mach cases.

Concerning the transport equation of the pseudo-viscosity in the SA-Neg. turbulence model, also expressed at the same spatial order as the other equations, the iterative convergence of its residual is generally very slow, even when the forces converge smoothly.

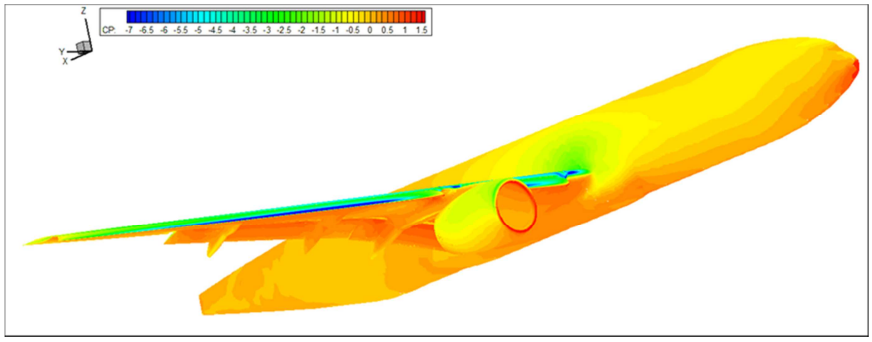

Fig. 11 cp field aoa 19.57°

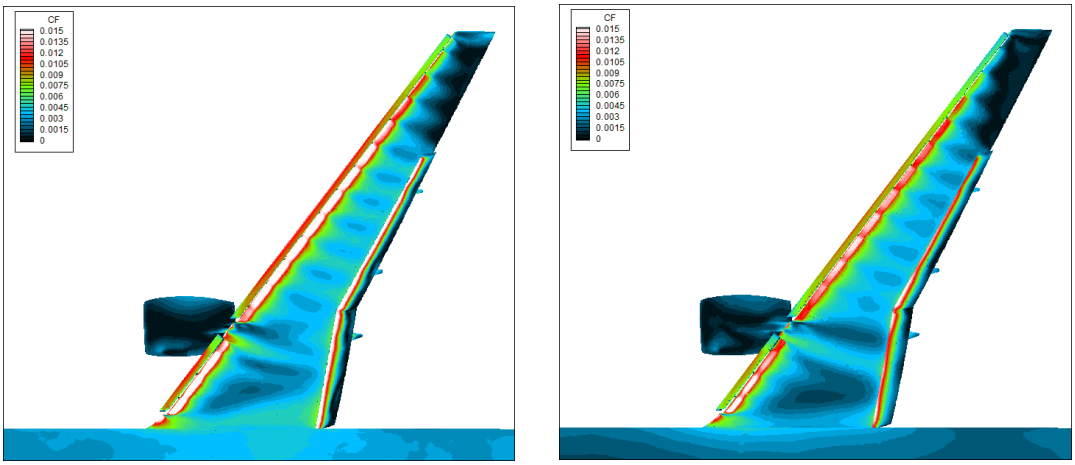

Fig. 12 fields of cf, aoa 7.05° on cell-vertex grid, 6.9 and 21 Mdof

The iterations are not pursued beyond a reduction of 4 orders of magnitude of the mass equation, the forces are then converged correctly with a k1 reconstruction, (see Fig. 7), while they continue to fluctuate and drift slowly for the 3rd order scheme, as shown on Fig. 13c.

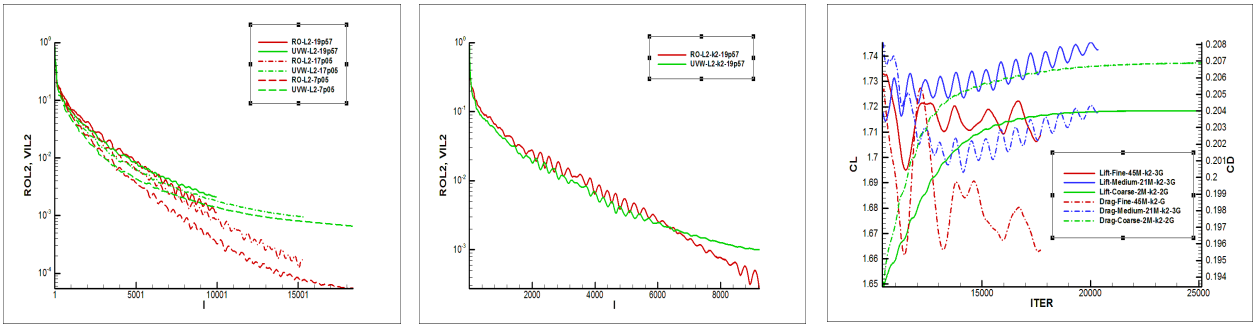

a b c

Fig. 13 Convergence of the rms residuals of mass and momentum. k1 (a), k3 (b); Iterative convergence of lift and drag in HO runs on 3 different grid configurations, 7.05° incidence (c)

Only the solution on a very coarse grid with 2 Mdof on only 2 active grids converges well in Fig. 13c. The forces computed on finer grids oscillate and would need excessive numbers of iterations in order to eventually stop these oscillations.

It is evidenced that this 3rd order solution lacks maturity at this stage. This prototype FV HO solver only provided a stable spatial integration process late during the workshop, and an implicit linearized version needs to be developped in order to verify the gains expected from this novel spatial integrator.

V. Test case 1b (grid convergence)

All these computations were done on the coarse, medium and fine P-T Q2 grids, with k2-k3 reconstructions. They use 2, 3 and even 4 overset active grids.

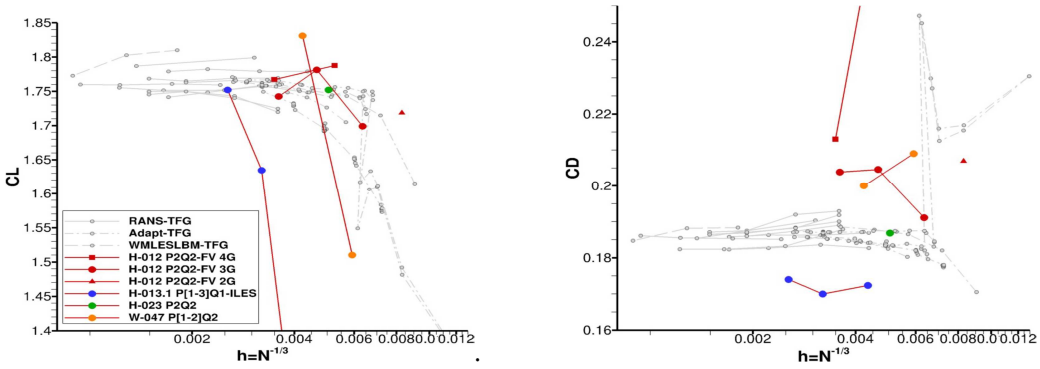

Figure 14 Lift and Drag at the nominal incidence, function of the number of dof/eqn N.

Fig. 14 comes from the summary report of the HO TFG [4] [6], the NextFlow ITW results are in red, with the label H-012, P2, hence 3rd order and Q2. They were done on 3 to 23 Mdof grids. In the background, the results from the other groups, RANS, WMLES, HybridLES, ADAPT are plotted.

The evaluation of the lift in the NextFlow computations is correct, event in the coarse 2G run (triangle), but they lack a consistent convergence, a run with a higher count of dofs should be necessary to confirm the trend. The drag however is always too high, like in other runs of the HO group using the y+ 100 to y+ 800 grids.

The improvement of these results requires the extension of the HO spatial integration to thinner grids in the wall region, without necessarily increasing the total count of dofs, since from these last results it appears that the coarse or medium surface grids might be sufficient to elevate the thin wall region grids.

On Fig. 15 we have plotted the computed cp profiles on the 3 overset grids from the fine P-T Q2 of Pointwise, together with the measured profiles corrected by the experimenters from the wind tunnel to the free stream conditions.

The plane slice is at 5% of wing span. The abscissa is made non dimensional successively by the chord of each wing element. The 3 grid computed solutions overlap over most of the element chords, they only tend to differ near the sharp trailing edges or discontinuities in the aerodynamics surface tangent planes. Compared to the experimental solution, the computed flow does not seem to re-attach downstream the main element.

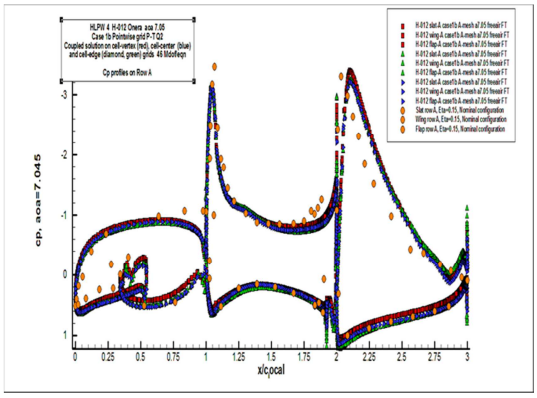

Fig. 15 Detailed comparison of cp profile in the plane slice A with the experimental results

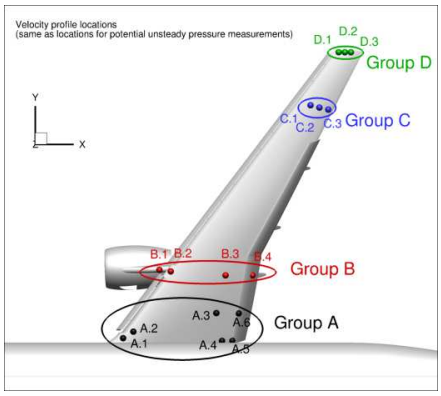

Fig. 16 Position of the unsteady pressure taps

The comparison of the results submitted to the workshop is also done on the velocity profiles computed over a number of pressure taps shown on Fig. 16. We present on Fig. 17 the velocity and pressure profiles over the groupA of taps, from the NextFlow run on the medium y+ 100 grid assembly. The computations are conducted with dimensional conservative variable fields in atmospheric conditions, so the pressure is in Pa, while velocity is made non dimensional in the post processing tool.

Contrary to the other plots, where the solutions on each active grid were shown individually, we have chosen to extract only one curve over each tap for all the active grids. One point is generated when the vertical line over the tap intersects any FV interface in all overset grids. The curve has wiggles until all the active grid solutions converge to a smooth overset field.

Detailed cross-comparisons of the solvers solutions were done in the workshop summary, we only discuss here some qualitative physical interpretations of the NextFlow results.

The pressure profiles over the taps A.3 and A.4 (blue and black curves, Fig. 17 B) are very different from the other ones, they do not show a strong static pressure decrease towards the wall, since they are in a detached flow region. This is confirmed by the velocity profiles on Fig. 17 A.

The taps A.5 and A.6 at the flap leading edge (orange and pink) are below a very thin accelerated flow region followed by a lower velocity zone which is the wake of the main element (see Fig. 17A). The cp decrease towards the wall at A.5 is very intense, over a short distance.

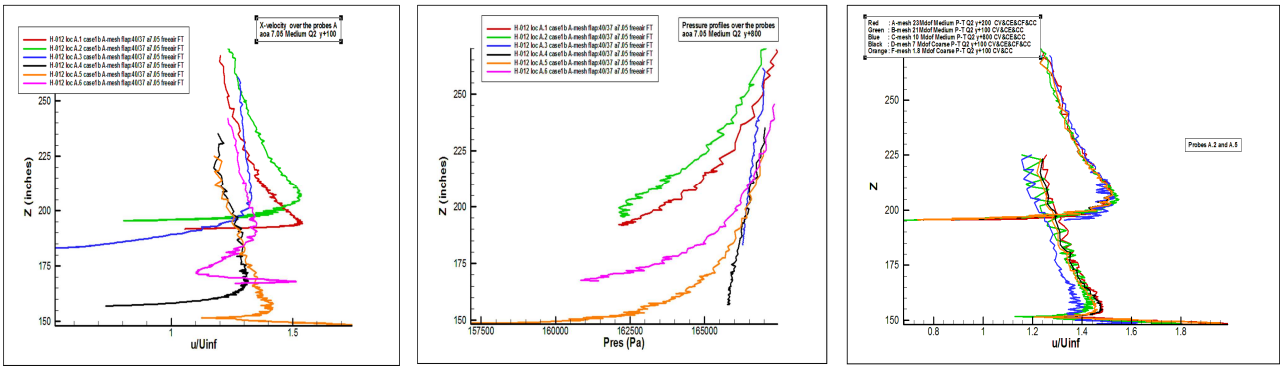

A B C

Fig. 17 Velocity and pressure profiles over the pressure taps of row A (see Fig. 16).

On Fig. 17 C the velocity profiles over the taps A.2 and A.5 are drawn. They are obtained with 5 different grids of this convergence case 1b. All the y+ 100 and y+200 solutions are close to each other, only the solution computed over the medium y+ 800 grid (blue curve) differs close to the wall and has wiggles that indicate difficulties in converging through the overset grids. The different velocity profiles between the taps A.5 (lower Z) and A.2 in terms of boundary layer thickness are captured on all grids.

VI. Qualitative views of the 3D fields

Some plots highlight the evolution of the solution in a given slice for different angles of attack of the flow.

Fig. 18 represents the increase in Mach number in the slat region when the incidence varies from 7.05° to 19.47°.

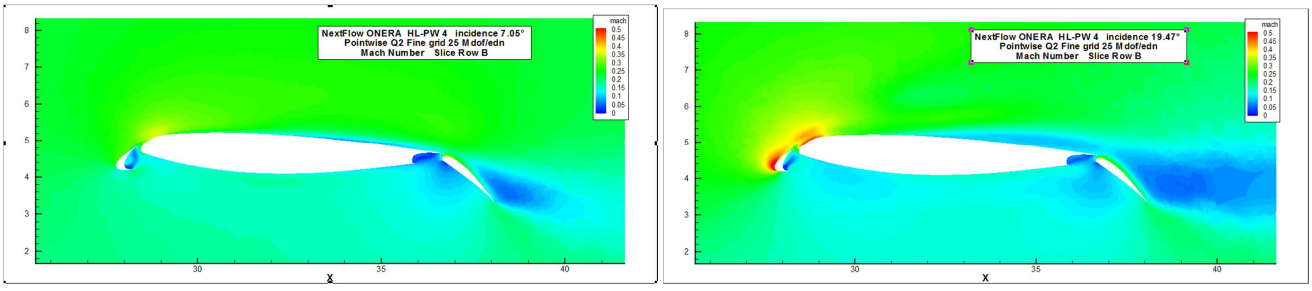

Fig. 18 Field of Mach number in slice B; Fine grid y+100, 3G; 25 Mddl/eqn.

The vortex that is generated over the plate soldered outside the engine can be tracked in its trajectory. 2 qualitative views illustrate this in Fig.19, for 2 different overset associations (46 Mdof on the fine grids and 12 Mdof on the medium ones) and 2 different angles of incidence, where the vorticity is plotted in the cell vertex grid.

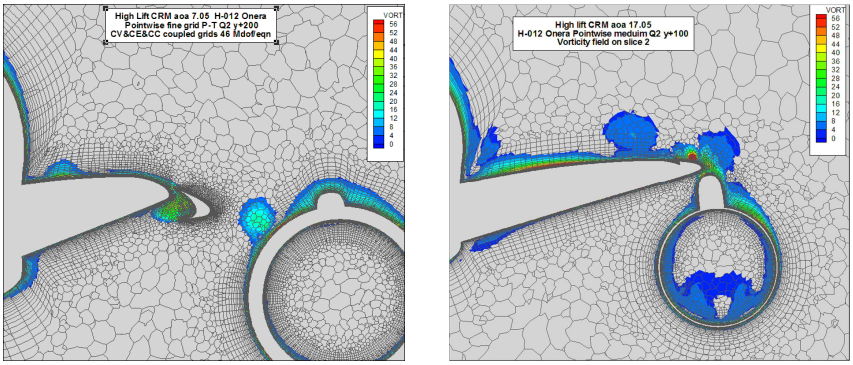

Fig. 19 Vorticity levels

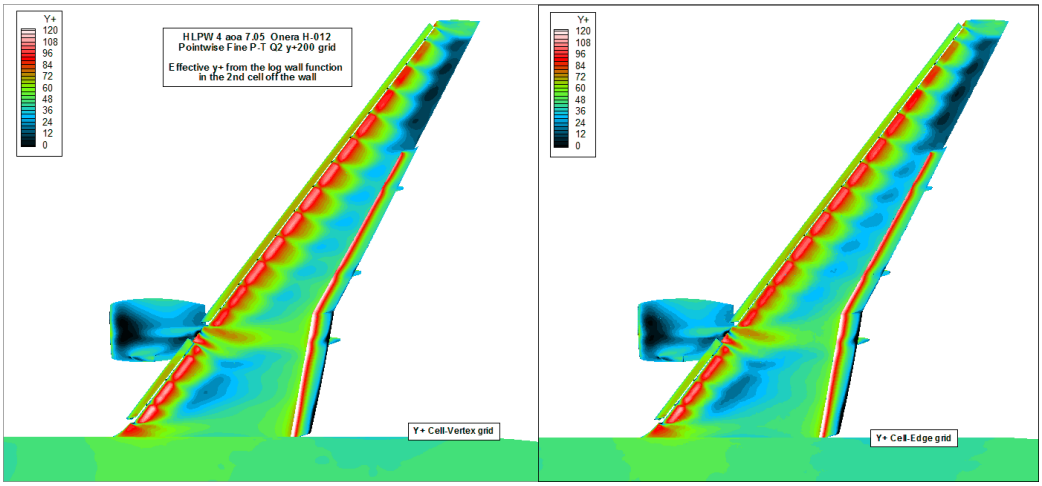

Fig. 20 Field of effective y+ obtained from the log law of the wall; fine y+200 grid aoa 7.05°.

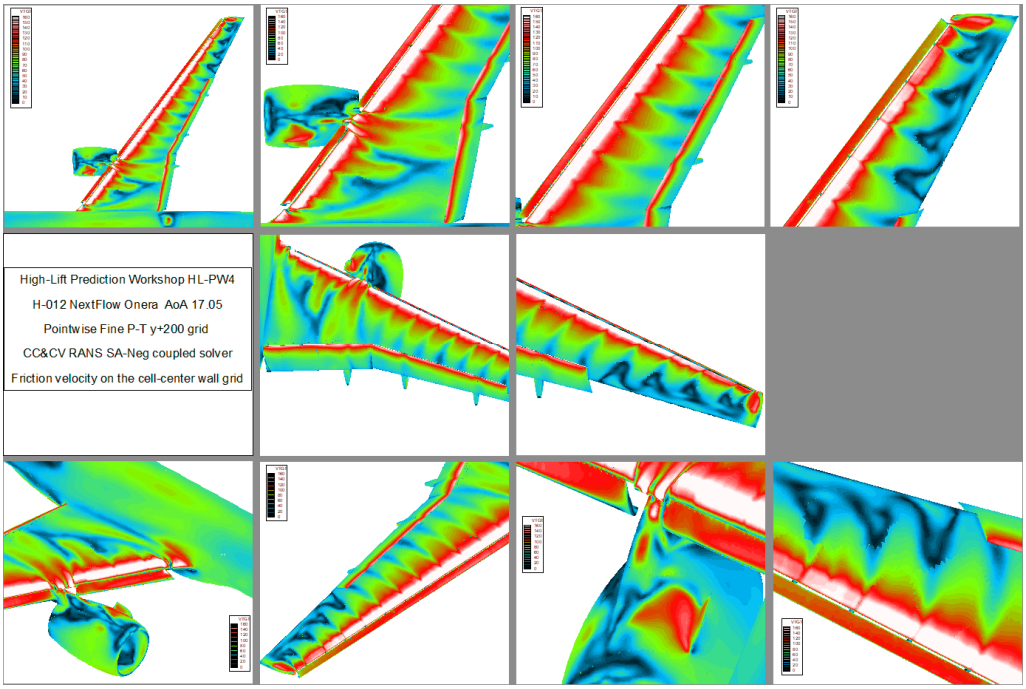

Fig. 21 Velocity modulus in the wall cell. Fine y+200 grid aoa 17.05°.

In order to check the validity of the thickness of the wall cells given by the y+ calculator of the POINTWISE mesh generator, we have plotted on Fig.20 the effective field of y+ as obtained when applying the log. wall function. In the computations, this wall function was applied either in the wall cell, or in the second one off the wall, depending if the wall boundary condition was expressed in strong or weak form (both were tested). The computed y+ is shown on the cell-vertex and on the cell-edge wall grids in the same computation. The objective y+ =200 level used in the mesh generator is never exceeded.

The velocity in the wall cell, which is used as an input to the wall function, provides a qualitative evaluation of the attachment of the flow. Wide detached flow regions are shown at 17.05° of incidence when plotting this velocity level (Fig. 21).

VII. Test case 3 (Verification case of the TMR web site)

These verification runs were done with an older version of the code, with the same coding of the Spalart-Allmaras Negative model. The 2D version only computes on the primal grid, made of a mixture of Q1 or Q2 quads and triangles, but it allows polynomial reconstructions up to degree 4. We used successively 2 families of grid, with y+ of the wall cell of the order of 1 or less, and numbers of cells from 166K to 500K.

The first one is obtained on the TMR web site of NASA [3], made of Q1 elements only, it was used by other Finite Volume RANS solvers (Fig. 22 A). The second one, made of quadratic quads, was generated by GRIDPRO for the workshop (Fig. 22 B). The flow conditions are Mach = 0.2, Reynolds 5M/chord, aoa 16°.

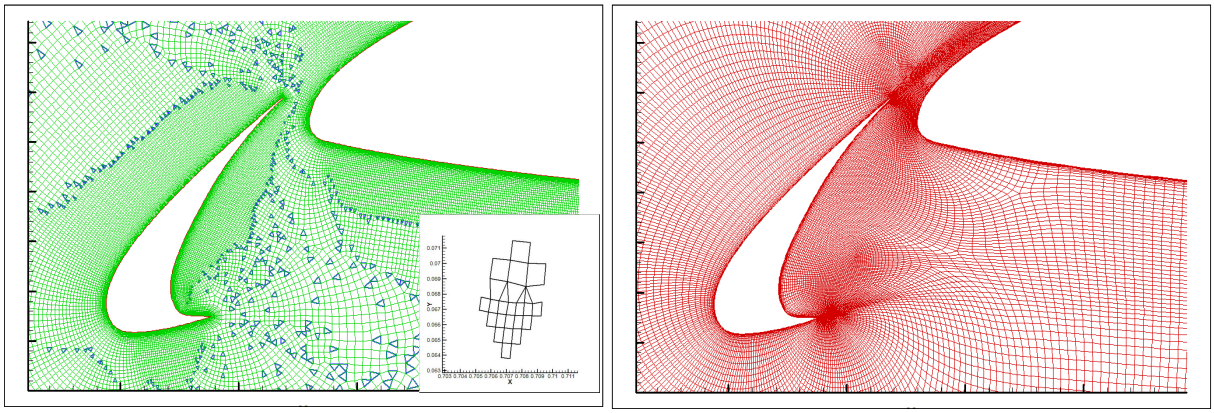

Fig. 22 A: Q1 tri-quads TMR ; L2 290 Kcells; Stencil k4. **Fig. 22 B: Q2 quads GRIDPRO; L3 166 Kcells.**

The cross-comparisons between the solvers use the lift and drag as function of the number of dof/eqn, and profiles of the velocity components and the turbulent viscosity in 3 vertical slices over the slat, the main element and the flap.

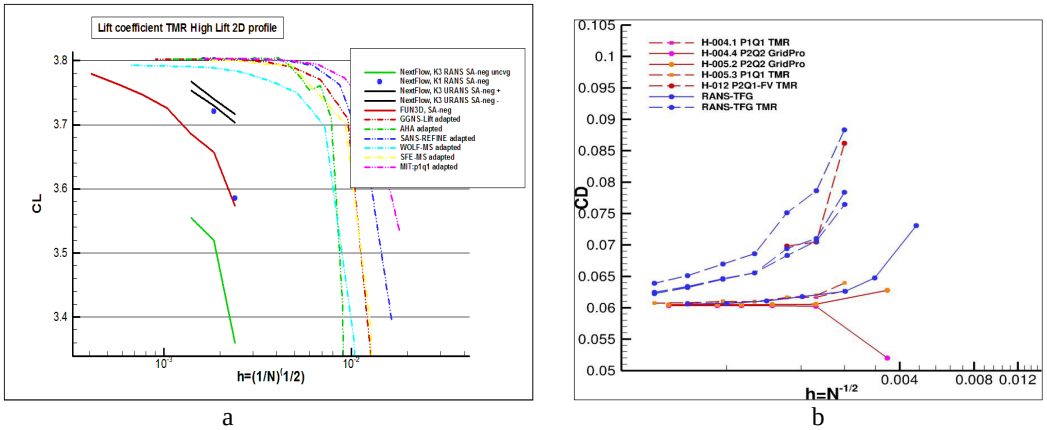

a b

Fig. 23 Lift figures (TMR results, a) **Drag figures (HLPW4 progress meeting, b)**

The NextFlow computations were done in a first step with the k1 multi-D reconstruction to keep close to the standard FV schemes. The lift results are shown on Fig. 23a, which was obtained from the TMR web site, and where the NextFlow results were added (2 blue dots for the k1 reconstruction). The drag results are plotted on Fig 23b, which was shown at the HLPW 4 progress meeting by the HO TFG coordinator (NextFlow results, in red dashed lines, are labelled H-012).

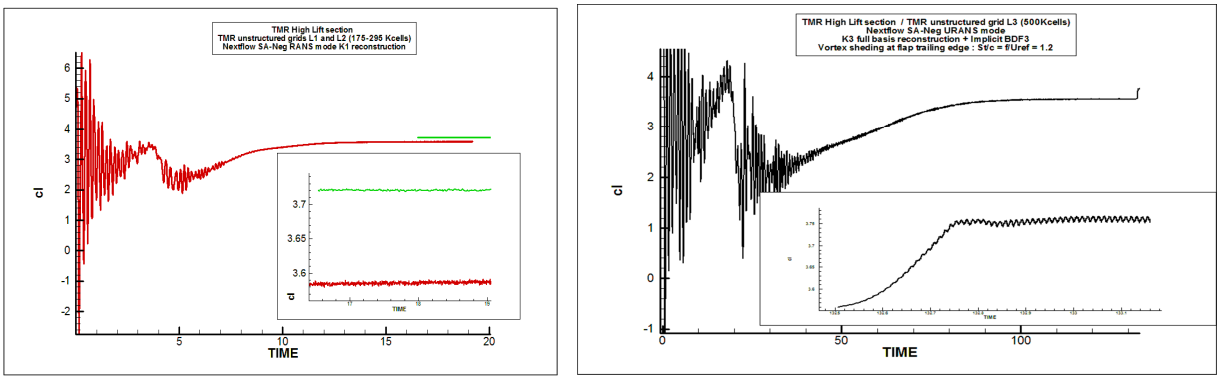

a b

Figure 24 : Iterative evolution of Lift on TMR grids; k1 reconstruction RANS (a), k3 RANS + URANS (b)

The k1 solution converged uniformly, towards a lift coefficient of 3.59 on the L1 grid of 175 Kdof and 3.72 on the L2 grid of 295 Kdof (see Fig. 24a). These results are satisfactory, when compared to the 2nd order FV reference on the same grids, while more accurate results of Fig. 23a, obtained for lower dof counts, used adaptive meshing algorithms.

However, the 3 runs with a k3 reconstruction on grid levels L1, L2 L3 do not converge, the residuals remain high and the lift cannot exceed very low values (see Fig. 24b RANS for the L3 grid), these values are reported as the green curve on Fig. 23a. The runs were then continued in URANS mode (Fig. 24b), with all the caution needed for this. The main concern in 2D is that the unsteady fluctuations, if any, will alter the velocity gradients and vorticity that are computed for the source in the transport equation of pseudo-viscosity in the SA-Neg model. The whole set of equations needs to be taken as unsteady.

This unsteady scheme uses a non-linearized time implicit solver, with inner iterations in each time step by local pseudo-time stepping and RK3 stages. The real time derivative is represented by BDF3 finite difference formulas.

The URANS solution is restarted at time 132.5, then an instability appears, the non-linear effects limit its amplitude and the lift coefficient fluctuates with a low amplitude of the order of +- 0.01 around a higher average than the RANS solution. The black curves of Fig. 23 a represent the min and max values of the fluctuating lift computed on the L1, L2 et L3 grids (500 Kdof for the L3 grid). The average drag obtained in these 3 runs is plotted on Fig. 23b.

Owing to the higher order of the implicit time derivative, only 12 time steps over the captured period of fluctuation are found necessary. This permits a high number of inner pseudo-time stepping iterations with a local stability criterion, in each physical time step (800 to 1600).

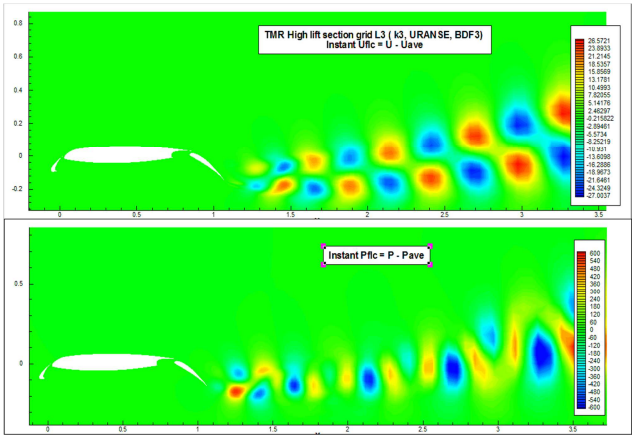

Fig. 25 Instant fields of velocity and pressure fluctuation

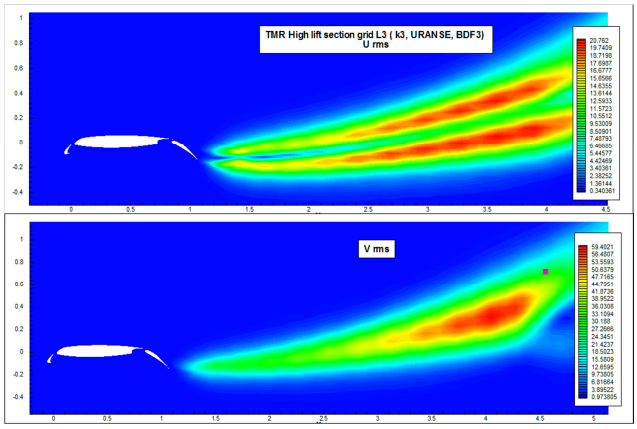

Fig. 26 rms values of the velocity fluctuations u',v'

The Strouhal number of the resulting vortex shedding on the flap, that can be visualized on Fig. 25 and 26, is found to be St = f*c*sin(α) /Uref = 0,35. Fig. 25 shows instant fields of the fluctuating component of velocity and pressure, in m/s and Pa, and Fig. 26 the rms of the 2 components of velocity, also in m/s, computed on the finest grid L3.

Fig. 27 shows respectively the averages over a cycle of pressure and the product of the 2 fluctuating components of velocity u'v'. Fig. 28 presents the turbulent viscosity fields, shown with the same levels as the results presented on the TMR site. The gain in lift brought by the URANS solution (middle and bottom views) can be evidenced by comparing the flow deflection with the RANS result. The region of high turbulent viscosity over the flap is also visually less thick.

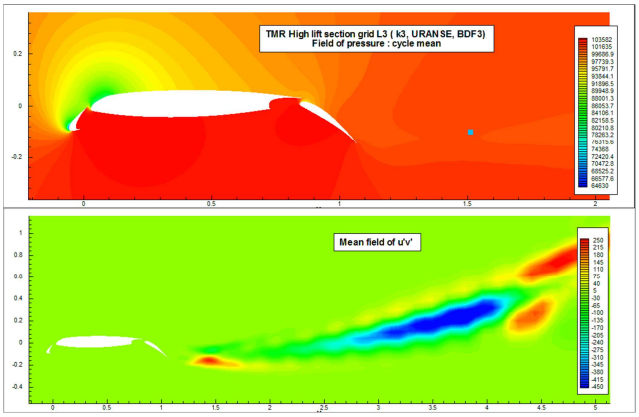

Fig. 27 Mean fields of pressure and the product of the fluctuating velocity components

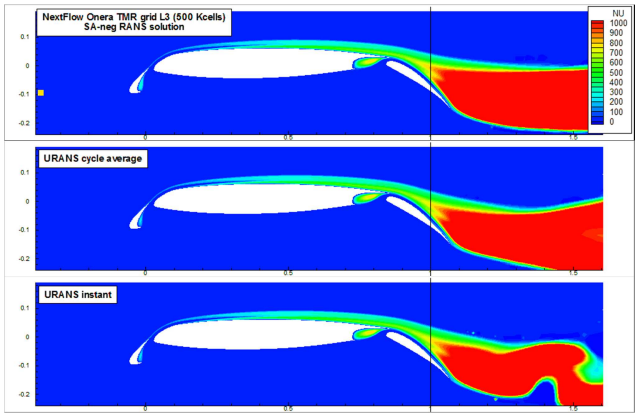

Fig. 28 Fields of turbulent viscosity A: RANS solution, B: URANS average, C: URANS instant

The unsteadiness that develops in the URANS computations with these higher order spatial and time schemes was confirmed by runs on the GRIDPRO meshes. All the computations done on these grids L2 to L4, from 195K to 396Kdof, either with the Q2 or Q1 assumption, led to unsteady solutions. The Q1 grids are the same as the Q2 ones, only the additional Q2 nodes are not considered and linear quads integration formulas used.

The Strouhal numbers and the amplitude of fluctuations are very close to those computed on the Q1 TMR grids. This is shown on Fig. 29. Only the solution on the very coarse grid L1 converged to steady state, although the unsteady implicit resolution and 3rd order FV schemes were also applied to it.

The mean lift is higher than the reference value of 3.8 from the steady RANS solvers on the L4 grid, which is not surprising since a new physical phenomenon is present in the solution. An instant field of entropy on this L4 grid is presented on Fig. 30.

The physical or simply numerical existence of this vortex shedding of small amplitude can be questioned, but no experiment could decide in favor of it. Its capture by a numerical scheme is certainly difficult, since it occurs in a region where the turbulent viscosity (Fig. 28) is very high, and also in consequence the turbulent diffusion of momentum. But the high shear and inflexion in the velocity profiles that are responsible for a sharp rise in turbulence levels over the flap can also generate the vortex shedding (see fig. 31, bottom-left). The fact that it was encountered on 2 families of different grids and across different refinement levels makes it credible.

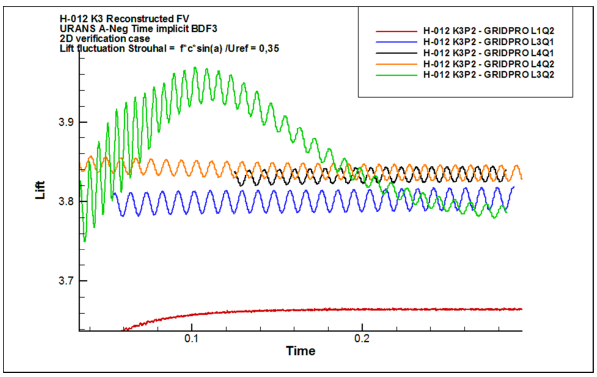

Fig. 29 Lift computed on GRIDPRO meshes, dt 0.001

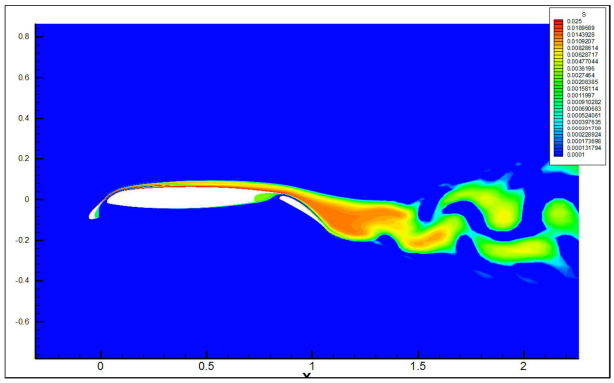

Fig. 30 Instant field of entropy, GRIDPRO L4

Results were submitted for the comparison of the profiles of velocity components and turbulent viscosity. The time averaged URANS solution were used, but since the vortex shedding occurs after 20% of the flap chord, the abscissa of the 3 profiles are in steady flow regions. Independently of the comparisons reported by the workshop and TFG coordinators, we compare our results on the finer TMR and GRIDPRO meshes to recent reference solutions computed by FUN3D on the TMR L7 grid, presented on the TMR web site. Results of 4 runs are shown on Fig. 31.

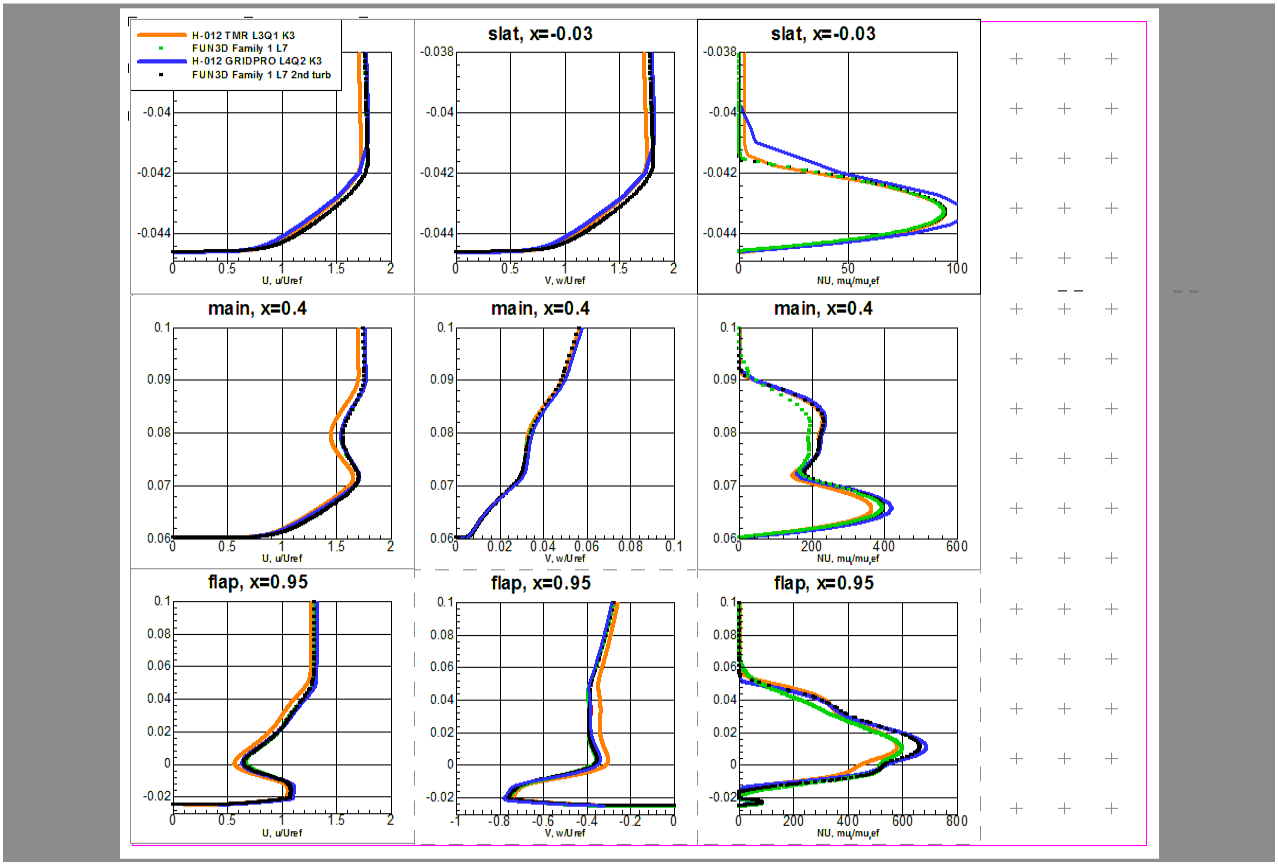

Figure 31 Profiles of velocity components and turbulent viscosity over 3 1D vertical slices.

The NextFlow solutions are in orange (TMR finer grid) and blue (GRIDPRO finer mesh). The reference solution of FUN3D is in black, it has been improved with respect to the green solution of the same code by using a 2nd order scheme also for the transport equation of the pseudo-viscosity.

Our solution on the GRIDPRO mesh predicts too high a level of turbulent viscosity on the slat (top right), it is due to too coarse a grid in the normal direction to the slat, in comparison to the grid around the other elements The very thin boundary layer (0.002 chord) covers only the thickness of 6 cells here. All the other profiles computed on this GRIDPRO L4 grid are very close to the reference values, the turbulent viscosity profiles on the main and the flap capture also the wake of the upstream elements.

The differences with FUN3D are essentially limited to the thickness of the laminar region over the flap boundary layer (0 turbulent viscosity close to the wall on the bottom right figure). The results of NextFlow on the TMR grid are somewhat less accurate.

VIII. Conclusion

On the occasion of the High Lift Prediction Workshop 4, new developments in a 3D Unstructured Finite Volume solver were conducted, in order to increase the spatial order of the RANS scheme and to test coupling mechanisms between the solutions computed on the primal multi-element grid and its duals.

This overset coupling scheme showed correct convergence properties when using a linear reconstruction scheme, and an acceptable CLmax study could be conducted with these settings, in view of the lack of maturity of this numerical method. However, higher order spatial reconstructions are still challenging the present explicit iterative scheme.

Due to the complexity of the geometry of the HLPW4 test cases that has a direct impact on that of the grids, and since different flow features appear in various regions of space, a robust linearized implicit solver seems necessary to confirm the gain in accuracy from these recent space integration and overset coupling methods.

IX. Acknowledgements

The author would like to thank the organizers of the Workshop and the coordinators of the HO Technology Focus Group for their involvement in this task and their appreciated advice during the bi-weekly meetings. A special thanks is expressed to Steve Karman for the hard work he did to produce these quadratic grid in a wide variety of refinement levels and well-tailored to the needs of the TFG members.

References

[1] Le Gouez, J.M., "High-Order Finite Volume Method for Gas Dynamics on geometrically HO multi-element unstructured grids", AIAA paper 2020-1788, SciTech 2020, 6-10 January 2020, Orlando, USA.

[2] Le Gouez, J.M., "High-Order Overset Interpolation via Weighted Least-Square Polynomial Reconstruction for Finite Volume CFD", AIAA Paper 2016-2051, SciTech 2016, 4-8 January 2016, San Diego, USA

[3] NASA « Turbulence Modeling Resources »: https://turbmodels.larc.nasa.gov/multielementverif.html

[4] HO Technology Focus Group of HLPW 4: https://hiliftpw.larc.nasa.gov/Workshop4/TFGlist.html

[5] High Lift Prediction Workshop 4: https://hiliftpw.larc.nasa.gov/Workshop4/testcases.html

[6] Galbraith, M. and Karman, S.,"HLPW-4/GMGW-3: High Order Discretization Technology Focus Group Workshop Summary", AIAA Aviation Paper to appear, 2022.